PNAS RESEARCH ARTICLE | MICROBIOLOGY

Deciphering and targeting the pathogenic circuit of nonlytic hepatitis E virus infection using macrophage-augmented organoids

Kuan Liu[a,b,1,2], Yilan Zhao[c,1], Yang Wang[c], Theano Tsikari[d,e], Dewy Mae Offermans[c], Xincheng Li[b,c], Valeria V. Orlova[d,e], Luc J. W. van der Laan[b,f], and Qiuwei Pan[c,2]

Affiliations are included on p. 10.

Edited by Xiang-Jin Meng, Virginia Polytechnic Institute and State University, Blacksburg, VA; received February 2, 2026; accepted April 13, 2026

The pathophysiology caused by nonlytic viral infections is complex, often driven by macrophage-mediated immune responses that lead to hyperinflammation and collateral tissue damage. To conceptualize this complexity, we propose a pathogenic circuit comprising three interconnected nodes: nonlytic infection, inflammation, and immune-mediated cell death. To investigate this circuit, we combined hepatitis E virus (HEV), a prototypical nonlytic RNA virus, and macrophage-augmented organoids (MaugOs) as an innovative model. Here, we report successful recapitulation of the pathogenic circuit induced by HEV infection in MaugOs. Nonlytic HEV infection triggered robust inflammatory responses and subsequent cell death involving pyroptosis, apoptosis, and necroptosis pathways. By pharmacologically targeting individual circuit nodes as well as individual cell death pathways, we have dissected their interactions and identified potential therapeutic targets. Finally, we developed multitarget strategies by simultaneously targeting two or three nodes through rational drug combinations to effectively disrupt the pathogenic loop. Collectively, these findings elucidate the architecture of the pathogenic circuit underlying nonlytic HEV infection in MaugOs and inform the development of innovative multitarget therapies for improved disease treatment.

hepatitis E virus | orgnaoids | macrophages | pathophysiology | therapeutic targeting

Significance

This study establishes a pathogenic circuit framework to conceptualize the pathophysiology of nonlytic viral infections. Using hepatitis E virus (HEV) and macrophage-augmented organoids as an innovative experimental system, we delineate three interconnected nodes of this circuit: namely nonlytic infection, inflammation, and immune-mediated cell death. We further demonstrate that rational drug combinations targeting two or all three nodes can effectively disrupt this pathogenic loop. These findings provide mechanistic insights into the pathophysiology of HEV infection and offer a foundation for developing multitarget therapeutic strategies, with potential relevance to other nonlytic viral infections.

Viral infections in host cells generally follow two major patterns: lytic and nonlytic, which are fundamental to viral life cycles and pathogenesis (1–3). In a lytic infection, the virus rapidly replicates within the host cell, resulting in cell lysis and release of progeny virions. In contrast, nonlytic infections initially preserve host cell integrity but exhibit more complex pathophysiology, driven largely by immune-mediated processes. Diseases associated with nonlytic infections often arise indirectly through dysregulated immune responses, leading to pathological inflammation and tissue damage (1, 2).

Hepatitis E virus (HEV), a hepatotropic pathogen, is a typical nonlytic virus that does not directly cause injury to infected liver epithelial cells (4–6). However, acute HEV infection, particularly in pregnant women, can lead to severe complications such as acute liver failure, miscarriage, preterm delivery, and stillbirth, even resulting in fatality (7). Severe liver inflammation in acute HEV infection is closely linked to immune dysregulation, with macrophages playing a central role. In pregnant women with acute hepatitis E, macrophage frequency is elevated in blood (8), along with increased levels of proinflammatory cytokines such as IFN-γ, TNF-α, IL-10, and IL-18, all associated with adverse outcomes (9, 10). Based on a patient cohort with acute HEV infection, as well as animal and cell culture models, we previously discovered that HEV robustly activates the NLRP3 inflammasome in macrophages (11, 12), which indirectly triggers injury of infected epithelial cells (13), highlighting a potential mechanism of HEV-induced hyperinflammation in severe cases.

This illustrates the complexity of pathophysiology caused by nonlytic viral infections driven by immune cells, macrophages in particular. The pathological inflammation triggers massive cell death, both of infected cells as well as noninfected bystander cells, thus causing (collateral) tissue damage. This creates a vicious cycle of cell death and damage-associated inflammation that can cause patient morbidity and mortality (14). Tissue damage implicated in viral pathogenesis is mainly driven by regulated cell death including three major pathways, pyroptosis, apoptosis, and necroptosis (15). Although early studies linked specific viral infections to distinct cell death mechanisms, accumulating evidence now indicates that this view is overly simplistic (16). In fact, all three pathways can be activated in parallel and may act coordinately during severe viral infections (17). This complex

Author contributions: K.L., V.V.O., L.J.W.v.d.L., and Q.P. designed research; K.L., Y.Z., Y.W., T.T., D.M.O., and X.L. performed research; V.V.O. contributed new reagents/analytic tools; K.L., Y.Z., L.J.W.v.d.L., and Q.P. analyzed data; and K.L. and Q.P. wrote the paper.

The authors declare no competing interest.

This article is a PNAS Direct Submission.

[1]K.L. and Y.Z. contributed equally to this work.

[2]To whom correspondence may be addressed. Email: kuanliu28@163.com or q.pan@erasmusmc.nl.

This article contains supporting information online at https://www.pnas.org/lookup/suppl/doi:10.1073/pnas.2603870123/-/DCSupplemental.

Published May 14, 2026.

pathogenesis explains the ineffectiveness of current antiviral therapies for severe viral diseases, which focus solely on the virus and do not address hyperinflammation or resulting cell death causing tissue injury (18).

To develop effective treatment for these patients requires a deeper understanding of disease mechanisms and the development of advanced therapeutic strategies. This in turn requires innovative experimental models. Immortalized cell lines, though widely used, have limitations that compromise their relevance for modeling virus–host interactions (19). Organoid technology offers a more physiologically relevant alternative, better replicating the architecture, diversity, and function of original tissues (20). However, classical tissue-derived organoids do not fully capture all aspects of disease seen in infected patients, particularly the inflammatory responses driven by immune cells such as macrophages (14). We recently have successfully established macrophage-augmented organoids (MaugOs), that primary human epithelial organoids are integrated with macrophages, to simultaneously model infection, the ensuing inflammatory response and injury (13, 21).

In this study, we aim to elucidate the pathogenic mechanisms of nonlytic infections through a proposed "circuit" concept, which proposes nonlytic infection, inflammatory response, and cell death as interconnected, self-regulating nodes within a pathogenic loop. Using HEV as a prototypical nonlytic virus and MaugOs as an innovative model, we will dissect the interactions among these nodes to uncover the mechanistic foundations of this circuit. We further identify promising therapeutic targets within the loop, to develop multitarget strategies for better treating nonlytic HEV infection.

Results

Recapitulating the Circuit of HEV Infection, Inflammatory Response, and Cell Death in MaugOs. HEV primarily infects hepatocytes (22), but can also target cholangiocytes in patients (23). We previously established HEV infection in primary organoids derived from the intrahepatic biliary compartment of the human liver (4), known as intrahepatic cholangiocyte organoids (ICOs) (24, 25). Because HEV is a nonlytic virus (5, 6), infection alone does not cause lysis of infected epithelial cells (4). However, in MaugOs that are incorporated with macrophages, we observed extensive induction of cell death (13). Building on these observations, this study conceptualizes HEV infection, inflammatory response, and cell death as three interconnected nodes forming a pathogenic circuit, which will be systematically investigated using the MaugO model (Fig. 1*A*).

We first inoculated ICOs with infectious HEV particles, a genotype 3 strain produced from Huh7 cells harboring the full-length p6 infectious clone (26, 27), and subsequently integrated THP-1 monocyte-derived proinflammatory macrophages to establish MaugOs. Visualization and quantification of cell death by propidium iodide (PI) staining and lactate dehydrogenase (LDH) release demonstrated that HEV infection in ICOs did not cause significant cell death (Fig. 1 *B* and *C*), confirming features of nonlytic infection. In contrast, HEV infection in MaugOs induced extensive cell death (Fig. 1 *B* and *C*), affecting both the organoid and macrophage compartments (Fig. 1*B*). Further quantitative analyses at 24 and 36 h after MaugO establishment revealed a time-dependent increase in viral RNA level (Fig. 1*D* and *SI Appendix*, Fig. S1*A*), and correspondingly elevated release of LDH (Fig. 1*E*) and proinflammatory cytokines (IL-1β and TNF-α) (Fig. 1 *F* and *G*), whereas such time-dependent responses do not occur in uninfected MaugOs (*SI Appendix*, Fig. S1 *B* and *D*).

These findings prompted us to examine three major forms of programmed cell death: apoptosis, necroptosis, and pyroptosis (15). We assessed the hallmarks of these three types of cell death in both HEV-infected (Fig. 1 *H–K*) and uninfected (*SI Appendix*, Fig. S1 *E–H*) MaugOs at 24 and 36 h by western blot analysis. Caspase-3, a key executor of apoptosis, was strongly and specifically activated in HEV-infected MaugOs at 24 and 36 h through cleavage (Fig. 1*H*). Pyroptosis, initiated by inflammasome activation and gasdermin D (GSDMD) cleavage (28), was indicated by detection of increased NLRP3 level (Fig. 1*I*) and GSDMD-N fragments (Fig. 1*J*), a hallmark of pyroptosis, in HEV-infected MaugOs. Necroptosis, mediated by receptor-interacting protein kinases RIPK1 and RIPK3 through phosphorylation of mixed lineage kinase domain-like pseudokinase (MLKL), was evident by robust MLKL phosphorylation (pMLKL) upon HEV infection (Fig. 1*K*). Collectively, these results demonstrate that HEV infection specifically and concurrently activates all three programmed cell death pathways in MaugOs.

To further refine the model, we constructed MaugOs using macrophages differentiated from human induced pluripotent stem cells (hiPSCs) (29), which express an H2B-GFP nuclear reporter for real-time tracking and visualization within the MaugO structure (Fig. 1*L*). Consistently, we confirmed HEV replication (Fig. 1*M*), releases of cell death marker LDH (Fig. 1*N*), and induction of proinflammatory cytokines IL-1β (Fig. 1*O*) and TNF-α (Fig. 1*P*) in these MaugOs. The presence of cleaved caspase-3 (Fig. 1*Q*) and pMLKL (Fig. 1*R*) was further confirmed by immunofluorescence staining. The infection and active replication of HEV were confirmed by detecting viral double-stranded RNA (dsRNA), the replication intermediate (Fig. 1 *Q* and *R*).

To further dissect the interactions, we cocultured HEV-infected organoids with macrophages in a trans-well system (*SI Appendix*, Fig. S2*A*). This resulted in significant increase of cell death in HEV-infected compared to uninfected organoid compartment (*SI Appendix*, Fig. S2 *B–D*), as well as viral transmission to macrophages as shown by qRT-PCR quantification of viral RNA (*SI Appendix*, Fig. S2*E*). HEV-infected organoids had altered morphology as shown by phalloidin staining (*SI Appendix*, Fig. S2*F*), as well as the presence of cleaved caspase-3 (*SI Appendix*, Fig. S2*G*) and pMLKL (*SI Appendix*, Fig. S2*H*) staining. In contrast, cleaved caspase-3 (*SI Appendix*, Fig. S2*I*) and pMLKL (*SI Appendix*, Fig. S2*J*) were hardly detectable in HEV-infected or uninfected macrophages.

Collectively, MaugOs are capable of recapitulating the circuit of HEV infection, inflammatory response, and cell death. Macrophages play a key role in the pathogenesis of the nonlytic infection potentially through both cell–cell contact and paracrine routes.

Targeting the Virus Node by Antiviral Drug. To further elucidate complex interplay between infection, inflammatory response, and cell death, and to define therapeutic targets, single-target approaches were applied to inhibit individual nodes while assessing their impact on the entire pathogenic circuit in HEV-infected MaugOs.

Ribavirin is a classical antiviral drug that has demonstrated anti-HEV activity in experimental models (30, 31) and clinical efficacy in patients with chronic hepatitis E (32). Treatment with ribavirin significantly and dose-dependently inhibits HEV replication in MaugOs (Fig. 2*A*), whereas the effects on inflammatory cytokine production (Fig. 2 *B* and *C*) and LDH release (Fig. 2*D*) were mild.

Targeting Inflammatory Response. Building on the critical role of NLRP3 inflammasome activation in HEV-driven inflammatory responses (11, 12), we employed MCC950 (Fig. 2*E*), a well-characterized pharmacological inhibitor of the NLRP3

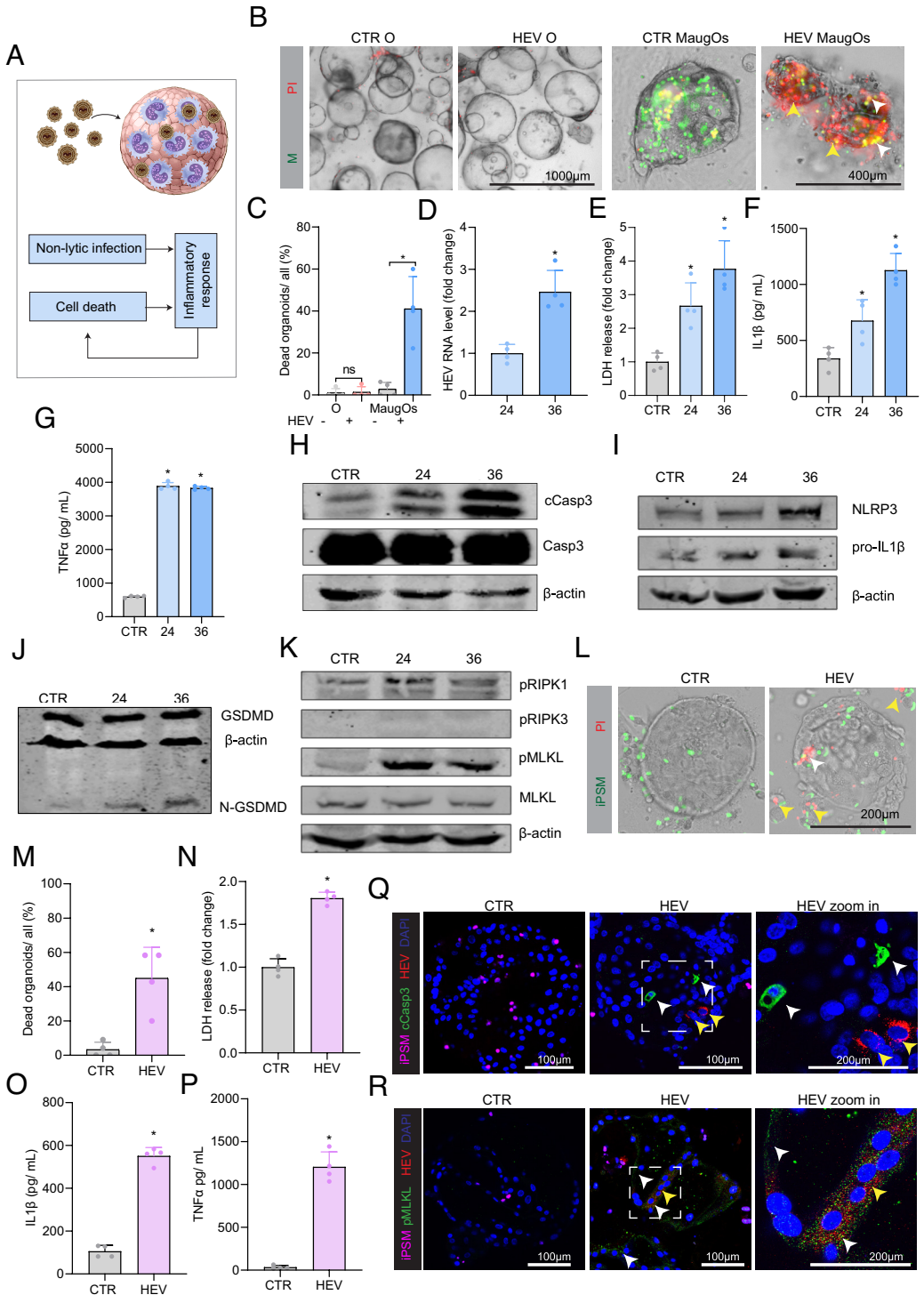

Fig. 1. Recapitulating the circuit of HEV infection, inflammatory response, and cell death in MaugOs. (*A*) Schematic illustration of the circuit of HEV infection, inflammation, cell death circuit in MaugOs. (*B* and *C*) Visualization and quantification of cell death in organoids (O; n = 4) and MaugOs (n = 4) using Propidium Iodide (PI; red) staining marking dead or dying cells, and CFSE prelabeled THP-1 macrophages (M, green), at 36 h after MaugO assembly. White arrows indicate dying macrophages (yellow), whereas yellow arrows indicate dying organoid cells (red). (*D*) Quantification of HEV viral RNA in MaugOs at 24 and 36 h (n = 4). MaugOs with HEV infection at 24 h served as control (normalized as 1). (*E*) Quantification of the cell death marker lactate dehydrogenase (LDH) release in HEV-infected MaugOs 24 and 36 h after MaugO assembly (n = 4). MaugOs without infection and cultured for 24 h served as control (CTR, normalized as 1). (*F* and *G*) Quantification of IL-1β and TNF-α cytokine production in supernatant by ELISA (n = 4). (*H*) Western blotting analysis detecting the total and cleaved caspase 3 in HEV-infected MaugOs. MaugOs without infection and cultured for 24 h served as control (CTR). (*I* and *J*) Western blot analysis detecting the components of pyroptosis including NLRP3, GSDMD, and N-GSDMD. (*K*) Western blot analysis of key necroptosis components, including phosphorylated RIPK1 (pRIPK1), phosphorylated RIPK3 (pRIPK3), MLKL, and phosphorylated MLKL (pMLKL). (*L* and *M*) Visualization and quantification of cell death in HEV-infected MaugOs integrated with hiPSC-derived macrophages using Propidium Iodide (PI; red) staining marking dead or dying cells (n = 4). These MaugOs are cultured for 36 h and used throughout the following experiments (*N*–*R*). (*N*) Measurement of LDH levels in HEV-infected MaugOs (n = 4). MaugOs without infection served as control (normalized as 1). (*O* and *P*) Quantification of IL-1β and TNF-α cytokine production by ELISA (n = 4). (*Q*) Immunofluorescence staining images of HEV by detecting the replication intermediate double-stranded RNA (dsRNA), and cleaved caspase3 (cCasp3). White arrows indicate apoptotic (cleaved caspase3-positive), whereas yellow arrows indicate HEV dsRNA signals. (*R*) Immunofluorescence staining images of HEV dsRNA, phosphorylated MLKL (pMLKL). White arrows indicate necroptotic cells (1R, pMLKL-positive), whereas yellow arrows indicate HEV dsRNA signals. Data are mean ± SD. *$P < 0.05$; **$P < 0.01$; ***$P < 0.001$; Mann–Whitney *U* test. "n" denotes the number of biological replicates.

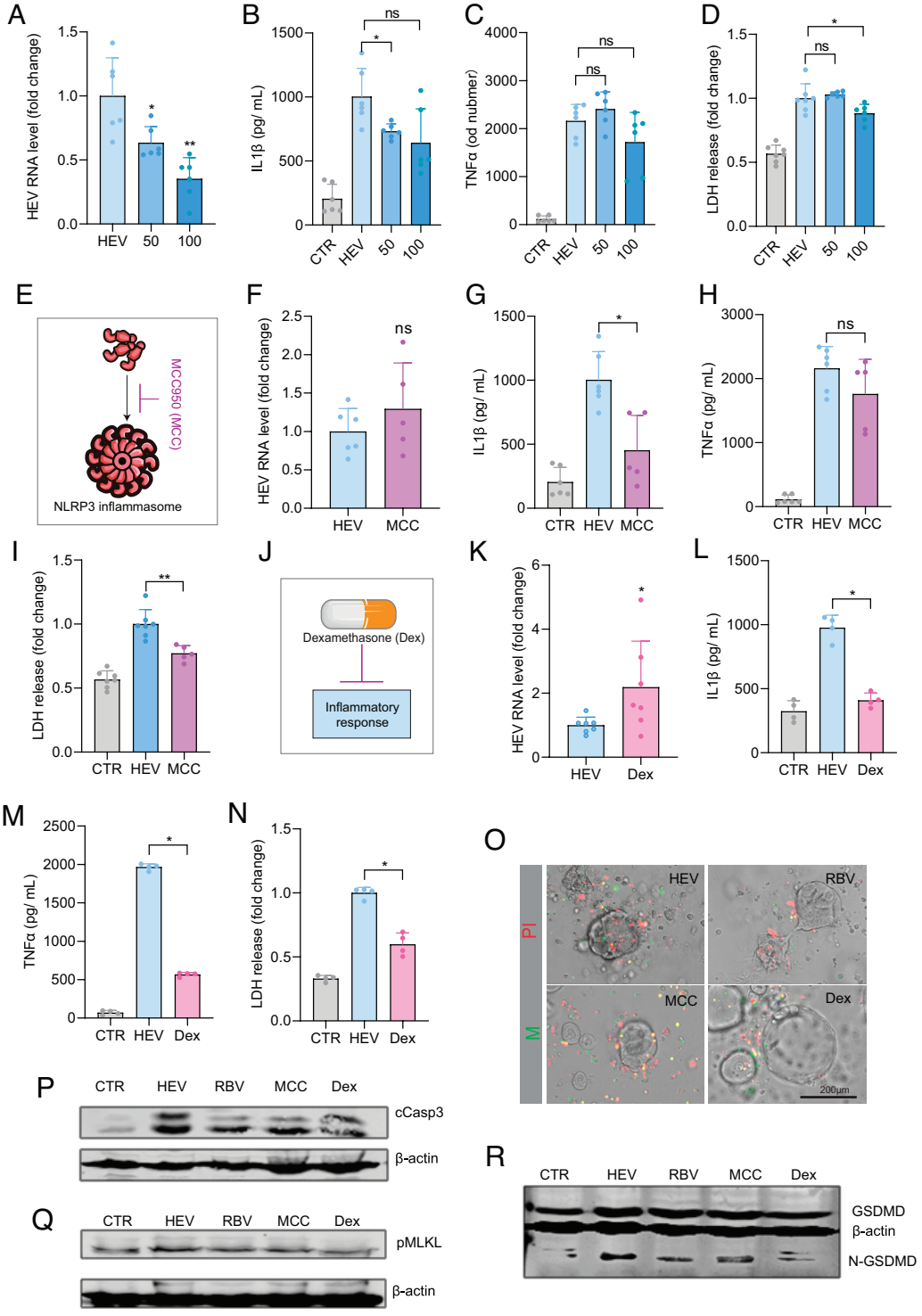

Fig. 2. Pharmacological targeting of HEV or inflammatory response. (*A*) Quantification of viral RNA in HEV-infected MaugOs (integrated with THP-1 macrophages) treated with 50 μM or 100 μM of the antiviral drug ribavirin (RBV) (n = 6). Viral RNA levels were quantified at 36 h after MaugO establishment. The infected but untreated MaugOs served as control (normalized as 1). (*B* and *C*) Quantification of IL-1β and TNF-α production in HEV-infected MaugOs treated with RBV (n = 6). (*D*) Quantification of lactate dehydrogenase (LDH) release in HEV-infected MaugOs treated with RBV (n = 6). (*E*) Schematic illustration of the NLRP3 inflammasome pathway and pharmacological targeting by the NLRP3 inhibitor (MCC950; MCC). The experiments were performed in parallel with Fig. 1*M*, and thus the CTR and HEV groups are shared with the groups of CTR and HEV in Fig. 1*M*. (*F*) The effects of NLRP3 inhibitor (MCC950; MCC) on HEV RNA level quantified by qRT-PCR in infected MaugOs (n = 6). The infected but untreated MaugOs served as control (normalized as 1). (*G* and *H*) Quantification of IL-1β and TNF-α production in HEV-infected MaugOs treated with MCC (n = 5). (*I*) Measurement of LDH release in HEV-infected MaugOs treated with MCC (n = 5). The infected but untreated MaugOs served as control (normalized as 1). The experiments shown in Fig. 2 *F–I* were performed in parallel with those in Fig. 2 *A–D*, and thus the CTR and HEV groups are shared. (*J*) Schematic illustration of anti-inflammatory drug dexamethasone (Dex). (*K*) Quantification of HEV viral RNA in HEV-infected MaugOs treated with Dex (n = 7). Viral RNA levels were quantified at 36 h after MaugO establishment. The infected but untreated MaugOs served as control (normalized as 1). (*L* and *M*) Quantification of IL-1β and TNF-α production in HEV-infected MaugOs treated with Dex (n = 4). (*N*) Measurement of LDH release in HEV-infected MaugOs treated with the Dex (n = 4). The infected but untreated MaugOs served as control (normalized as 1). (*O*) Visualization of cell death treated with RBV, MCC, and Dex using Propidium Iodide (PI; red) staining marking dead or dying cells. (*P–R*) The effects of the RBV, MCC, and Dex on cleaved caspase3 (cCasp3), phosphorylated MLKL (pMLKL), N-GSDMD in infected MaugOs. Data are mean ± SD. **P* < 0.05; ***P* < 0.01; ns: not significant; Mann–Whitney *U* test. n denotes the number of biological replicates.

inflammasome (33). Treatment of HEV-infected MaugOs with MCC950 did not affect viral replication (Fig. 2*F*) but significantly suppressed IL-1β production (Fig. 2*G*), a hallmark of inflammasome activation. TNF-α levels remained largely unchanged (Fig. 2*H*), whereas LDH release showed moderate reduction (Fig. 2*I*).

Considering that inflammasome activation may not be the sole driver of inflammation and aiming for clinical relevance, we next tested dexamethasone (Fig. 2*J*), a clinically approved anti-inflammatory drug (34). Unexpectedly, dexamethasone treatment significantly enhanced HEV replication in MaugOs (Fig. 2*K*). In contrast, it strongly suppressed the production of proinflammatory cytokines IL-1β (Fig. 2*L*) and TNF-α (Fig. 2*M*). Dexamethasone also markedly reduced cell death, as indicated by decreased LDH release (Fig. 2*N*) and PI staining (Fig. 2*O*). Western blot analysis of apoptosis, necroptosis, and pyroptosis markers revealed that treatment with ribavirin, MCC950, or dexamethasone lowered cleaved caspase-3 levels, while dexamethasone exerted the most pronounced inhibitory effect on pyroptosis, evidenced by reduced GSDMD-N levels (Fig. 2 *P–R*).

Targeting Cell Death Pathways. To target apoptosis, we treated HEV-infected MaugOs with Z-DEVD-FMK (Fig. 3*A*), an irreversible caspase-3 inhibitor. Unexpectedly, this treatment enhanced HEV replication (Fig. 3*B*) without producing clear effects on proinflammatory cytokine secretion (Fig. 3*C*) or LDH release (Fig. 3*D*). To inhibit pyroptosis, we employed VX765 (Fig. 3*E*), a selective caspase-1 inhibitor. VX765 treatment did not alter viral replication (Fig. 3*F*) but strongly suppressed IL-1β production (Fig. 3*G*), while leaving TNF-α levels unchanged (Fig. 3*H*) with moderately reduced LDH release (Fig. 3*I*). These results are consistent with those observed following treatment with the NLRP3 inhibitor MCC950 (Fig. 2 *E–I*).

To target necroptosis, we employed necrostatin-1, a RIPK1 inhibitor, and UH15-38, a RIPK3 inhibitor (Fig. 3*J*). Neither compound significantly affected viral replication (Fig. 3*K*); however, both profoundly suppressed TNF-α secretion while leaving IL-1β levels unchanged (Fig. 3*L*). Treatment also moderately reduced cell death, as indicated by decreased LDH release (Fig. 3*M*). Comparative analysis of these pharmacological inhibitors across the three programmed cell death pathways confirmed their specificity for their respective targets (Fig. 3 *N–Q*).

Multitarget Strategies to Disrupt the Pathogenic Circuit. As demonstrated above, single-target approaches, whether directed at the virus, the inflammatory response, or cell death, are insufficient to effectively control the pathogenic circuit of HEV infection. To overcome these limitations, we adopted a multinode targeting strategy designed to comprehensively block this circuit. This approach prioritizes the virus as the central node, given that viral replication is the primary initiating event. Building on the insights obtained, we developed rational drug combinations anchored by the antiviral agent ribavirin, complemented by additional interventions targeting inflammatory and cell-death pathways.

To simultaneously target viral replication and the inflammatory response, we tested a combination of ribavirin and dexamethasone. Ribavirin alone inhibited viral replication only, whereas dexamethasone alone promoted viral replication but suppressed cytokine production and LDH release. Importantly, only the combination treatment achieved concurrent inhibition of viral replication, inflammatory cytokine secretion, and cell death (Fig. 4 *A–C*). Similar response patterns were observed when ribavirin was combined with the pyroptosis inhibitor VX765 (Fig. 4 *D–F*) or the necroptosis inhibitor UH15-38 (Fig. 4 *G–I*).

Targeting all three nodes simultaneously requires more complex drug combinations. To provide proof-of-concept, we tested a combination of ribavirin, dexamethasone, and UH15-38 (Fig. 5*A*). In MaugOs integrated with THP-1 macrophages, this regimen achieved robust and concurrent inhibition of cell death (Fig. 5 *B–D*), HEV replication (Fig. 5*E*), and proinflammatory cytokine production (IL-1β and TNF-α; Fig. 5*F*). Western blot analysis confirmed suppression of hallmarks for apoptosis (cleaved caspase-3; Fig. 5*G*), necroptosis (pMLKL; Fig. 5*H*), and pyroptosis (N-GSDMD; Fig. 5*I*). We further validated this approach in MaugOs integrated with hiPSC-derived macrophages, where the combination consistently induced potent inhibition of cell death (Fig. 5 *J–L*), viral replication (Fig. 5*M*), and cytokine production (Fig. 5 *N* and *O*). Immunofluorescence staining visualized HEV infection (viral dsRNA; Fig. 5 *P* and *Q*), as well as reduced expression of apoptosis (cleaved caspase-3; Fig. 5*P*) and necroptosis (pMLKL; Fig. 5*Q*) markers.

Taken together, these findings demonstrate that rational drug combinations targeting two or three nodes of the circuit can effectively disrupt the pathogenic circuit of HEV infection (Fig. 6).

Discussion

This study frames infection, inflammatory response, and cell death as interconnected nodes forming a pathogenic circuit (Fig. 6). We focused on nonlytic infection and prioritized HEV as a model virus. However, this framework likely has broader implications for other nonlytic infections and potentially even certain lytic infections, which are interesting avenues for further investigation. Many viral diseases, in particular severe acute infections caused by lytic or nonlytic viruses, are critically shaped by hyperinflammation and tissue damage, in addition to the pathogen itself (35). Nevertheless, the exact features of this circuit are likely context-dependent, varying with virus type (RNA vs. DNA) and infection pattern (lytic vs. nonlytic). Future research expanding representative virus models will help comprehensively decipher this pathogenic circuit, offering a distinct perspective and foundation for developing advanced therapeutic strategies.

A unique strength of this study is the use of MaugOs, which allow a more physiologically relevant modeling of patient-like infections. Within MaugOs, HEV initially targets the epithelial compartment with productive infection and subsequently spreads to macrophages (4, 13), faithfully recapitulating the infection cascade and the associated inflammatory response and cell death. This level of complexity is not achievable with traditional single-cell-type models. By pharmacologically perturbing individual circuit nodes using antiviral drugs, anti-inflammatory agents, and cell death inhibitors, we dissected their interactions and identified promising therapeutic targets. Our primary focus was on macrophages, more specially representing macrophages derived from infiltrating monocytes, since these innate immune cells have been recognized as key drivers of hyperinflammation during severe viral infections (14). Liver-resident macrophages, mainly Kupffer cells, perform critical homeostatic and immunological functions, particularly in capturing circulating pathogens, most notably bacteria (36). It would be valuable to investigate whether Kupffer cells exhibit similar or distinct responses during viral infection, given their different developmental origin and functional profile compared to monocyte-derived macrophages. However, obtaining primary Kupffer cells from healthy human liver tissue is logically and ethically challenging, which limits their routine use in experimental virology studies. Future work using hiPSC-derived Kupffer cell models may help address this important question.

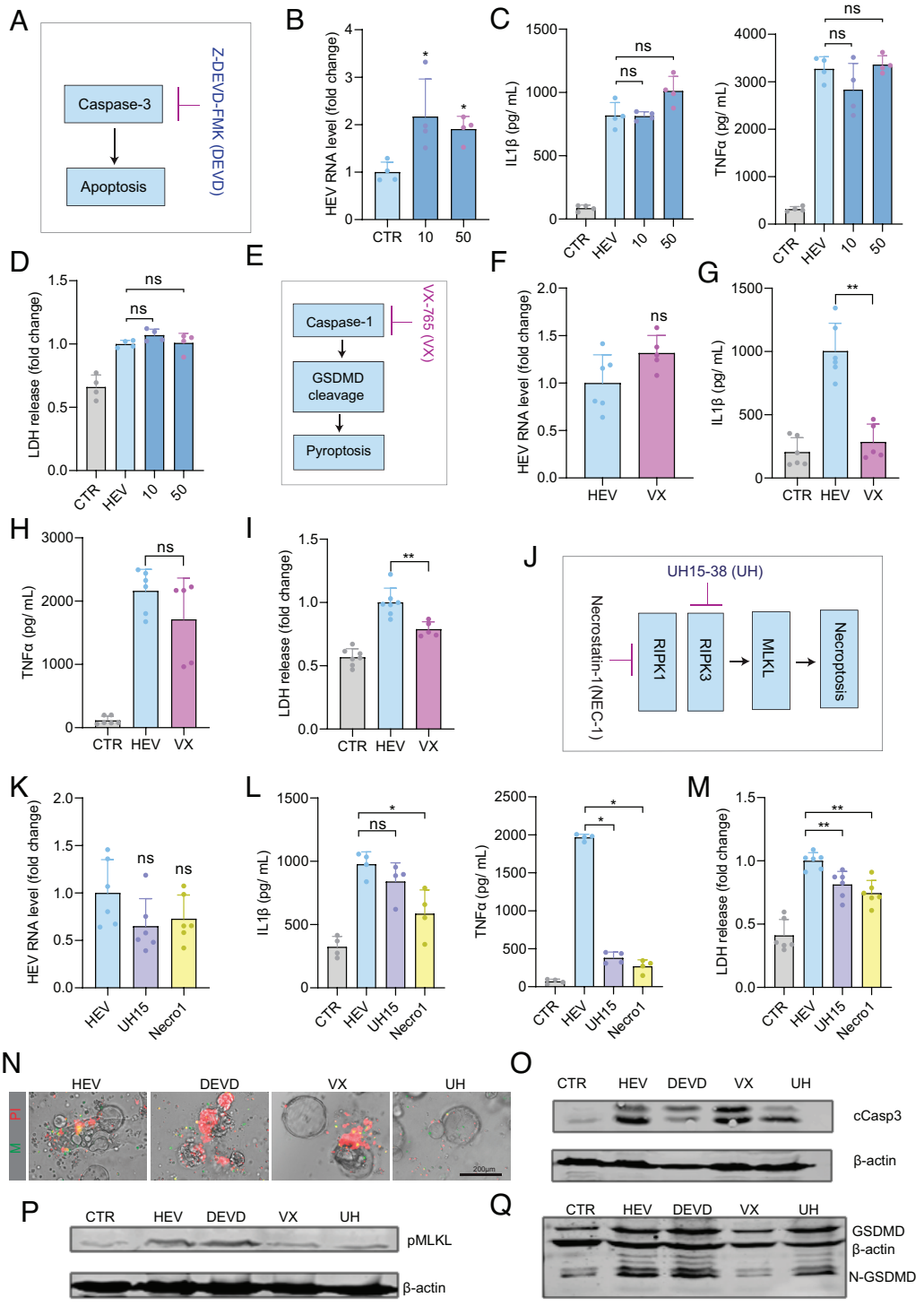

Fig. 3. Pharmacological targeting of cell death pathways. (*A*) Schematic illustration of the caspase-3–dependent apoptosis pathway and pharmacological targeting by Z-DEVD-FMK (DEVD). (*B*) Quantification of HEV viral RNA in HEV-infected MaugOs (integrated with THP-1 macrophages) treated with 10 μM or 50 μM DEVD (n = 4). Viral RNA levels were quantified at 36 h after MaugO establishment. The infected but untreated MaugOs served as control (normalized as 1). (*C*) Quantification of IL-1β and TNF-α production in HEV-infected MaugOs treated with DEVD (n = 4). (*D*) Quantification of lactate dehydrogenase (LDH) release in HEV-infected MaugOs treated with DEVD (n = 4). (*E*) Schematic illustration of the caspase-1–dependent pyroptosis pathway and pharmacological targeting by VX-765 (VX). (*F*) The effects of VX765 (VX) on HEV RNA level quantified by qRT-PCR in infected MaugOs (n = 5). Viral RNA levels were quantified at 36 h after MaugO establishment. The infected but untreated MaugOs served as control (normalized as 1). (*G* and *H*) Quantification of IL-1β and TNF-α production in HEV-infected MaugOs treated with VX (n = 5). (*I*) Measurement of LDH release in HEV-infected MaugOs treated with VX (n = 5). The infected but untreated MaugOs served as control (normalized as 1). The experiments shown in Fig. 3 *F–I* were performed in parallel with those in Fig. 2 *F–I*, and thus the CTR and HEV groups are shared. (*J*) Schematic illustration of the necroptosis pathway and pharmacological targeting by the RIPK1 inhibitor Necrostatin-1 (Nec-1) or the RIPK3 inhibitor UH15-38 (UH). (*K*) Quantification of HEV viral RNA in HEV infected-MaugOs treated with Nec-1 20 μM or UH 1 μM (n = 6). Viral RNA levels were quantified at 36 h after MaugO establishment. The infected but untreated MaugOs served as control (normalized as 1). (*L*) Quantification of IL-1β and TNF-α production in HEV-infected MaugOs treated with Nec-1 or UH (n = 4). (*M*) Measurement of LDH release in HEV-infected MaugOs treated with Nec-1 or UH (n = 6). The infected but untreated MaugOs served as control (normalized as 1). The experiments shown in Fig. 3 *K–M* were partially performed in parallel with those in Fig. 2 *K–N*, and thus some CTR and HEV groups are partially shared. (*N*) Visualization of cell death treated with DEVD, VX, or UH on using Propidium Iodide (PI; red) staining marking dead or dying cells. (*O–Q*) The effects of the DEVD, VX, or UH on cleaved caspase3 (cCasp3), phosphorylated MLKL (pMLKL), N-GSDMD in HEV-infected MaugOs. Data are mean ± SD. *$P < 0.05$; **$P < 0.01$; ns: not significant; Mann–Whitney *U* test. n denotes the number of biological replicates.

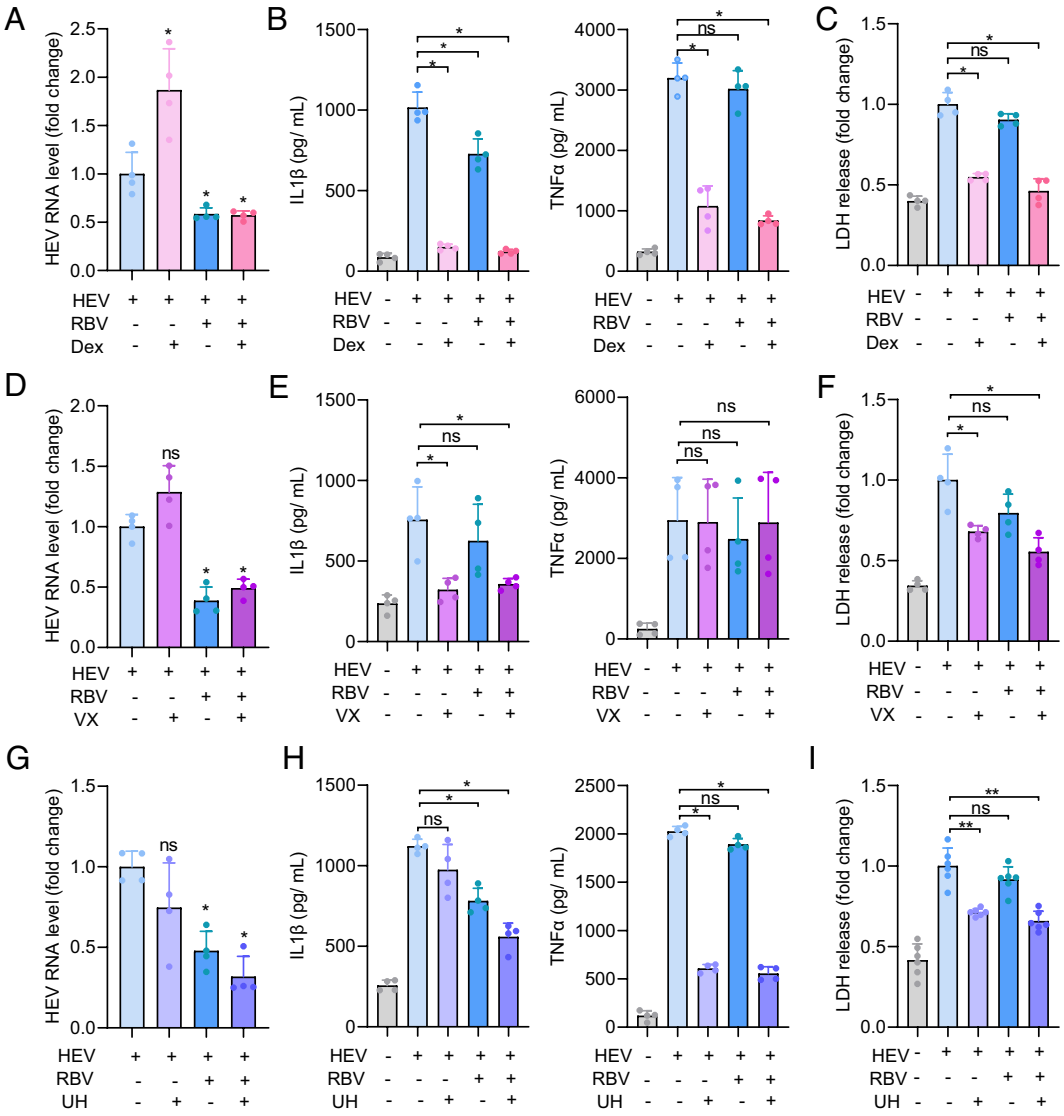

Fig. 4. Simultaneously targeting two nodes of the circuit. (*A*–*C*) Quantification of HEV viral RNA, IL-1β, TNF-α production, and lactate dehydrogenase (LDH) release in HEV-infected MaugOs (integrated with THP-1 macrophages) treated with the antiviral drug ribavirin (RBV), the anti-inflammatory drug dexamethasone (Dex) or the combination (n = 4). (*A* and *C*) Quantifications were performed 36 h after MaugO establishment. The infected but untreated MaugOs served as control (normalized as 1). The experiments shown in Fig. 4*B* were performed in parallel with Fig. 3*C*, and thus CTR groups are shared. (*D*–*F*) Quantification of HEV viral RNA (n = 4), IL-1β, TNF-α production, and LDH release in HEV-infected MaugOs treated with the antiviral drug ribavirin (RBV), the caspase-1 inhibitor (VX), or the combination (n = 4). (*D* and *F*) The infected but untreated MaugOs served as control (normalized as 1). (*G*–*I*) Quantification of HEV viral RNA (n = 4), IL-1β, TNF-α production (n = 4), and LDH release (n = 6) in HEV-infected MaugOs treated with the antiviral drug ribavirin (RBV), the RIPK3 inhibitor (UH), or the combination. (*G* and *I*) The infected but untreated MaugOs served as control (normalized as 1). Data are mean ± SD. **P* < 0.05; ***P* < 0.01; ns: not significant; Mann–Whitney *U* test. n denotes the number of biological replicates.

Other immune cell types, such as T and B lymphocytes of the adaptive immune system, also play critical roles in viral pathogenesis. However, integrating adaptive immune cells into organoid systems and eliciting appropriate responses remains technically challenging. Recent advances have demonstrated the feasibility of integrating adaptive immune cells, such as the construction of human intestinal immuno-organoids incorporating autologous T cells (37). Furthermore, immune organoids derived from human lymphoid tissues exhibit hallmark features of adaptive immunity, including antibody responses to viral antigens (38, 39). Continued development of immune-competent organoids will enable more comprehensive modeling of complex virus–host interactions and elucidation of pathogenic mechanisms. These innovations position organoids as a transformative component of New Approach Methodologies, offering animal-free experimentation with high physiological relevance (40).

In HEV-infected MaugOs, treatment with the NLRP3 inhibitor or dexamethasone potently suppressed IL-1β production, a hallmark of inflammasome activation. Interestingly, notable differences were observed. For example, dexamethasone, but not the NLRP3 inhibitor, inhibited TNF-α production and promoted HEV replication. These disparities suggest that HEV-induced inflammation involves mechanisms beyond inflammasome activation, as the broad-spectrum anti-inflammatory effects of dexamethasone extend to multiple pathways. The distinct mechanisms driving viral inflammation warrant further investigation (41).

We observed activation of three major programmed cell death pathways, namely pyroptosis, apoptosis, and necroptosis, in HEV-infected MaugOs. This observation aligns with the emerging concept of PANoptosis, an inflammatory programmed cell death pathway characterized by coordinated crosstalk among pyroptosis (P), apoptosis (A), and necroptosis (N) (42, 43). PANoptosis has

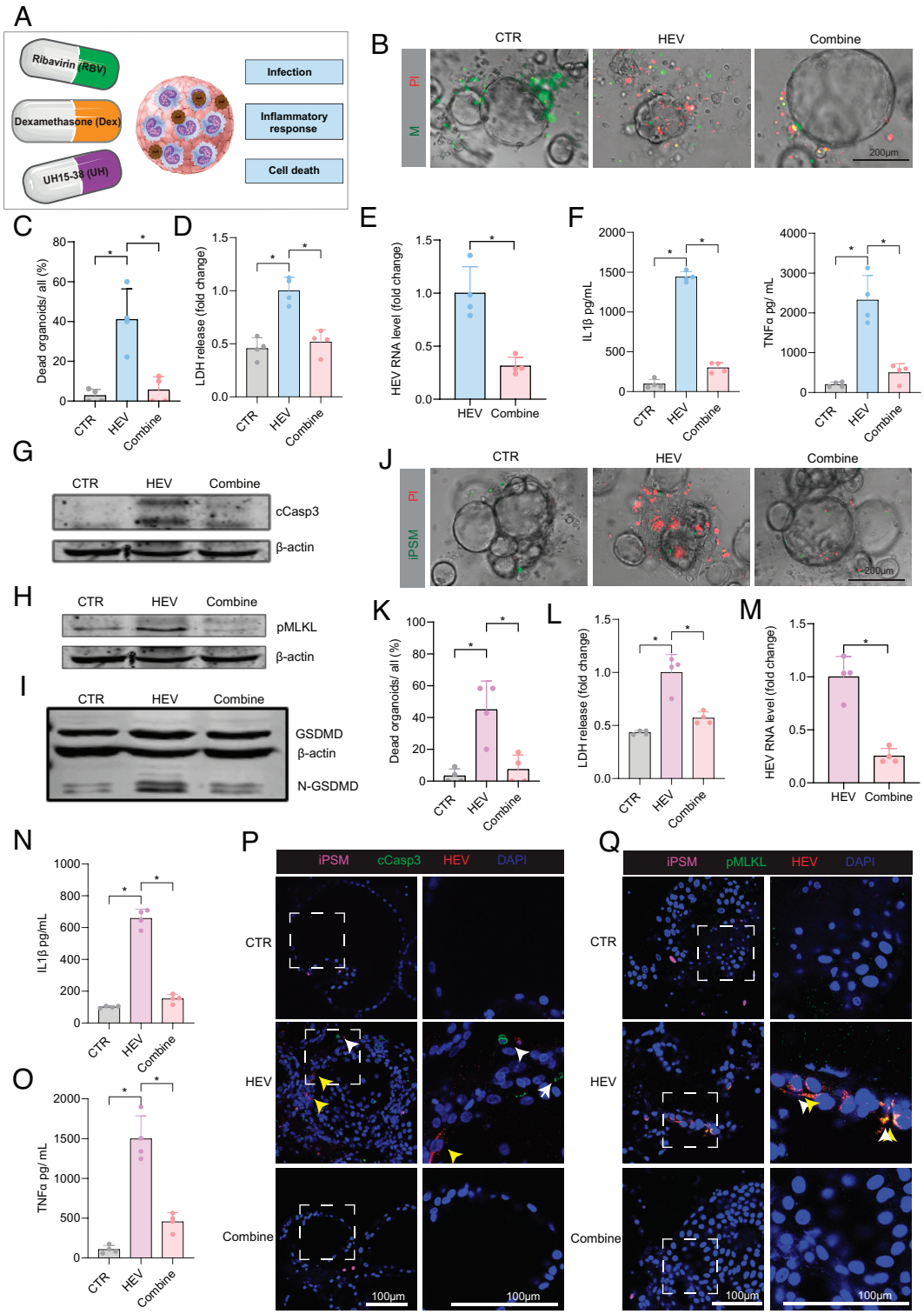

Fig. 5. Simultaneously targeting all three nodes of the circuit. (*A*) Schematic illustration of the combination therapy using ribavirin (RBV), dexamethasone (Dex), and UH15-38 (UH) targeting viral infection, inflammatory responses, and cell death. Quantifications were performed 36 h after MaugO establishment. (*B* and *C*) Visualization and quantification of cell death in MaugOs (integrated with THP-1 macrophages) treated with the RBV, Dex, and UH combination using Propidium Iodide (PI; red) staining to label dead or dying cells (n = 4), The experiments were performed in parallel with Fig. 1*C*, and thus the CTR and HEV groups are shared with the groups of MaugOs with or without HEV in Fig. 1*C*. (*D*–*F*) Quantification of HEV viral RNA, IL-1β, TNF-α production, and lactate dehydrogenase (LDH) release in HEV infected MaugOs treated with the RBV, Dex, and UH combination (n = 4). (*D* and *E*) The infected but untreated MaugOs served as control (normalized as 1). (*G*–*I*) The effects of RBV, Dex, and UH combination on cleaved caspase3 (cCasp3), phosphorylated MLKL (pMLKL), N-GSDMD in HEV-infected MaugOs. Fig. 5 *G* and *H* show different target proteins detected on the same membrane and share the same β-actin. (*J* and *K*) Visualization and quantification of cell death in MaugOs integrated with hiPSC-derived macrophages (GFP marked; green) by PI staining (red) to label dead or dying cells (n = 4). The experiments were performed in parallel with Fig. 1*M*, and thus the CTR and HEV groups are shared with the groups of CTR and HEV in Fig. 1*M*. These MaugOs are used throughout the following experiments (*L*–*Q*). (*L*–*O*) Quantification of HEV viral RNA, IL-1β, TNF-α production, and LDH release in HEV-infected MaugOs treated with the combination (n = 4). (*L* and *M*) The infected but untreated MaugOs served as control (normalized as 1). (*P*) Immunofluorescence staining images of HEV dsRNA, and cleaved caspase3 (cCasp3). (*Q*) Immunofluorescence staining images of HEV dsRNA, and phosphorylated MLKL (pMLKL). White arrows indicate apoptotic (5*P*, cleaved caspase3-positive) or necroptotic cells (5*Q*, pMLKL-positive), whereas yellow arrows indicate HEV dsRNA signals. (*C*–*F* and *K*–*O*) Data are mean ± SD. **P* < 0.05; ***P* < 0.01; ****P* < 0.001; Mann–Whitney *U* test. n denotes the number of biological replicates.

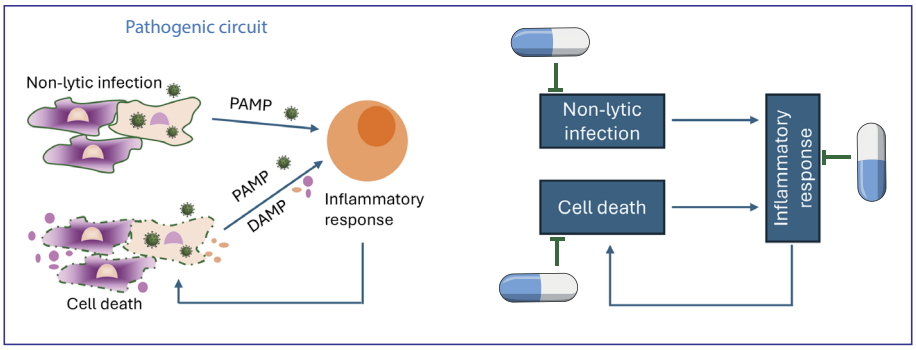

Fig. 6. Schematic illustration of the pathogenic circuit underlying nonlytic viral infections. The circuit defines infection, inflammation, and cell death as three key nodes. The virus does not kill infected cells, but PAMPs (Pathogen-Associated Molecular Patterns; e.g. viral DNA /RNA) released can activate inflammatory response, which then causes cell death, release of DAMPs (Damage-Associated Molecular Patterns), and tissue damage. Therapeutic interventions can be designed to target any single node of the circuit or to simultaneously modulate two or all three nodes to achieve improved outcomes.

been shown to play a critical role in macrophages during influenza A virus infection (43). A notable distinction, however, is that PANoptosis has primarily been defined within a single cell type, whereas our MaugO model captures coordinated cell death involving both epithelial and immune cells. These processes may occur in parallel or partially overlap with the evolving concept of PANoptosis, suggesting a broader, multicellular dimension to inflammatory cell death in organ systems.

Ribavirin, a broad-spectrum antiviral drug, has been widely used off-label for chronic hepatitis E treatment (32). However, its clinical efficacy in severe acute HEV infection remains uncertain (44, 45). Anti-inflammatory corticosteroids such as dexamethasone have shown benefit in hospitalized COVID-19 patients with acute SARS-CoV-2 infection (34). Nevertheless, such treatment can enhance viral replication (46), a phenomenon we also observed in HEV-infected MaugOs. Recently, the RIPK3-targeting cell death inhibitor UH15-38 was reported to partially reduce lung inflammation and prevent mortality following influenza A virus infection, although it did not inhibit viral replication (47). These findings are largely in line with the single-target approaches that we tested in HEV-infected MaugOs. To overcome the limitations of single-target approaches, we demonstrate the advantages of multitarget strategies to effectively disrupt the pathogenic circuit underlying HEV infection. This was achieved by rational drug combinations that simultaneously target multiple nodes, using ribavirin as the backbone since viral replication represents the primary initiating event.

This study has several limitations. First, only one viral model was used; future research should extend these findings to other pathogenic viruses. Second, macrophages were the only immune cell type incorporated into the organoids. The inclusion of additional immune cell types and investigation of their roles in viral pathogenesis remain important next steps. Third, in addition to western blot analysis demonstrating three types of cell death in HEV-infected MaugOs, immunostaining provided robust visualization of apoptosis and necroptosis using antibodies against cleaved caspase-3 and pMLKL. Unfortunately, the antibody against N-GSDMD remains technically challenging for staining to visualize pyroptosis. Finally, many of the pharmacological inhibitors employed in this study are not yet clinically applicable, and quantitatively comparing numerous drug combinations poses technical challenges, in addition to the limitation posed by the lack of in vivo validation. Therefore, the emphasis of this work is on overarching strategies that simultaneously inhibit infection, inflammatory responses, and cell death, rather than on defining specific therapeutic regimens.

Collectively, by employing innovative experimental models, this study elucidated the dynamic interactions among three interconnected nodes within the pathogenic circuit of HEV infection, suggesting a perspective that shifts from a virus-centric view toward an integrated host–pathogen framework for understanding viral diseases. Furthermore, it highlights the therapeutic potential of multitarget strategies, demonstrating proof-of-concept for their superiority over single-target approaches in developing next-generation treatments for severe viral infections, thereby warranting further investigation.

Methods

Virus. Plasmid construct containing the full-length HEV genome (Kernow-C1 p6 clone; GenBank Accession Number JQ679013) was transcribed into genomic RNA by enzyme-digested and linearized plasmid DNA using mMessage mMachine T7 RNA kits (Invitrogen) (27). Next, genomic RNA was introduced into Huh7 by electroporation as previously described to produce infectious HEVs in vitro (4, 11).

Organoid Culture. Tissue specimens (≤0.5 cm^3) were obtained from donor liver biopsies during liver transplantation procedures performed at the Erasmus Medical Center Rotterdam and were used for subsequent organoid isolation and culture. The study was approved by the Medical Ethical Council of Erasmus MC (MEC-2014-060), and written informed consent was obtained from all participants.

Human primary organoids, namely ICOs, were isolated and cultured according to previously established protocols (24). In brief, organoids were cultured in expansion medium (EM) based on advanced DMEM/F12 (Invitrogen), supplemented with 100 μg/mL primocin (Life Technologies), 0.01 M HEPES (Life Technologies), 200 mM ultraglutamine (Life Technologies), 1% (v/v) of N2 (Gibco), 2% (v/v) of B27 (Gibco), 1 mM N-acetylcysteine (Sigma-Aldrich), 10 mM nicotinamide (Sigma-Aldrich), 5 μM A83.01 (Tocris), 10 μM forskolin (Tocris), 10 nM gastrin (Sigma-Aldrich), epidermal growth factor (EGF) at 50 ng/mL (PeproTech), 10% (v/v) of R-spondin-1 (conditioned medium), fibroblast growth factor 10 (FGF10) at 100 ng/mL (PeproTech), hepatocyte growth factor (HGF) at 25 ng/mL (PeproTech). Detailed information is provided in *SI Appendix*, Table S1.

Macrophage Generation. Human monocytic THP-1 cells were cultured in RPMI 1640 medium supplemented with 15 ng/mL phorbol 12-myristate 13-acetate (PMA) at 37 °C for 48 h to induce macrophage differentiation. After washing with PBS, macrophages were stimulated with 100 ng/mL lipopolysaccharide (LPS) and 25 ng/mL interferon-γ (IFN-γ) for an additional 48 h to generate proinflammatory macrophages.

Generation of macrophages from hiPSCs was based on protocols established from a previous study (29). Briefly, monocytes were generated from a GFP-tagged hiPSC line obtained from the Allen Cell Collection. For macrophage differentiation, 0.75 × 10^6 monocytes were seeded onto FBS-coated wells and cultured in IMDM/F12 medium supplemented with nine factors (IF9S). IF9S consisted of IMDM (Invitrogen) supplemented with 50% F12 Nutrient Mix (Invitrogen), 10 ng/mL polyvinyl alcohol (Sigma), 0.1% chemically defined lipids

(Invitrogen), 2% insulin–transferrin–selenium-X (Invitrogen), 40 μL/L monothioglycerol solution (Sigma), 64 mg/L L-ascorbic acid 2-phosphate (Sigma), 2 mM GlutaMAX (Invitrogen), 1% nonessential amino acids (Invitrogen), and 0.5% penicillin–streptomycin.

The medium was supplemented with 80 ng/mL macrophage colony-stimulating factor (M-CSF; Sigma) and refreshed every 1 to 2 d. After 5 d of differentiation, macrophages were further stimulated with 10 ng/mL lipopolysaccharide (LPS) and 20 ng/mL interferon-γ (IFN-γ) for an additional 2 d to induce a proinflammatory macrophage phenotype. The medium was replaced to remove LPS and IFN-γ before assembling the macrophages with organoids to generate MaugOs.

Establishment of MaugOs and Virus Inoculation. Organoids were mechanically fragmented and incubated with cell culture–derived HEV particles (10^7 copies/mL) for 6 h at 37 °C. During the inoculation period, organoids were gently resuspended every 30 min. Following inoculation, organoids were centrifuged at 300× g for 5 min at 4 °C and the supernatant was removed. Organoids were subsequently washed three times with advanced DMEM/F12 to remove residual virus and embedded in Matrigel for culture at 37 °C with 5% CO2 for 24 h. Uninfected organoids cultured under identical conditions served as controls.

After incubation, HEV-infected or uninfected organoids were mechanically fragmented into small pieces and integrated with macrophages in Matrigel-precoated culture wells to generate MaugOs. MaugOs were collected at the indicated time points after establishment for subsequent analyses.

Transwell Coculture of Organoids and Macrophages. Following a 6-h inoculation with HEV particles, organoids were embedded in Matrigel and maintained in the lower compartment of a transwell system. Macrophages were seeded onto 0.4 μm semipermeable transwell inserts (Corning BV) and cocultured with organoids for 24 or 48 h. Control groups were processed in parallel under identical conditions without viral exposure.

RNA was isolated from macrophages collected from the transwell inserts. For immunofluorescence analysis, macrophages or organoids were fixed and stained for phosphorylated MLKL (p-MLKL) or cleaved caspase-3 in combination with double-stranded RNA (dsRNA), detecting the HEV replication intermediate.

Enzyme-Linked Immunosorbent Assay (ELISA). The concentrations of IL-1β and TNF-α in the culture supernatants of MaugOs were quantified using commercially available ELISA kits according to the instructions of manufacturers. IL-1β levels were measured using an ELISA kit from BD Biosciences, while TNF-α concentrations were determined using a TNF-α ELISA kit from Thermo Fisher Scientific (Cat# 88-7346-88).

LDH Release Measurement. The release of LDH into cell culture supernatant was assessed using the CytoTox 96® Non-Radioactive Cytotoxicity Assay Kit (Promega), following the manufacturer's recommended protocols. In brief, the supernatants of MaugOs were collected. The LDH activity in the culture supernatant was then measured at a 490 nm wavelength.

qRT-PCR Analysis of Gene Expression. Total RNA was isolated using the NucleoSpin RNA II Kit (Macherey-Nagel; Bioke, Leiden, the Netherlands). RNA concentration and purity were assessed with a NanoDrop ND-1000 spectrophotometer (Wilmington, DE, USA). qRT-PCR was performed using SYBR Green chemistry with the Applied Biosystems SYBR Green PCR Master Mix (Thermo Fisher Scientific Life Sciences) on a QuantStudio3 Real-Time PCR System (Thermo Fisher Scientific Life Sciences).

Gene expression levels were normalized to the housekeeping gene glyceraldehyde 3-phosphate dehydrogenase (GAPDH) and calculated using the $2^{-\Delta\Delta Ct}$ method ($\Delta\Delta Ct = \Delta Ct\_sample - \Delta Ct\_control$). Primer sequences are provided in *SI Appendix*, Table S2.

Immunoblot Analysis. Sample lysates were heated at 95 °C for 5 min and resolved by 10% sodium dodecyl sulfate–polyacrylamide gel electrophoresis (SDS-PAGE) at 90 V for 120 min. Proteins were then electrophoretically transferred onto polyvinylidene difluoride (PVDF) membranes (0.45 μm pore size; Thermo Fisher Scientific Life Sciences) at 250 mA for 120 min. Membranes were blocked with blocking buffer (LI-COR Biosciences) and incubated with primary antibodies overnight at 4 °C.

The following primary antibodies were used: anti-NLRP3 (1:1,000, rabbit), anti–IL-1β (1:1,000, rabbit), anti–gasdermin D (GSDMD; 1:1,000, rabbit), anti–cleaved gasdermin D (N-GSDMD; 1:1,000, rabbit), anti–MLKL (1:1,000, rabbit), anti–phospho-MLKL (pMLKL; 1:1,000, rabbit), anti-caspase-3 (1:1,000, rabbit), anti–cleaved caspase-3 (1:1,000, rabbit), anti–phospho-RIPK1 (pRIPK1; 1:1,000, rabbit), anti–phospho-RIPK3 (pRIPK3; 1:1,000, rabbit), and anti–β-actin (1:1,000, mouse). Detailed information is provided in *SI Appendix*, Table S1.

After three washes, membranes were incubated with IRDye-conjugated anti-rabbit or anti-mouse secondary antibodies (1:5,000; LI-COR Biosciences) for 1 h at room temperature. Following three additional washes, protein bands were visualized using Odyssey 3.0 software.

Immunofluorescence Staining and Confocal Imaging. MaugOs were seeded into Matrigel-precoated μ-Slide 8 Well chambers (ibidi GmbH, 80826). Samples were fixed with 4% paraformaldehyde (PFA) for 10 min at room temperature, washed with PBS, and permeabilized with 0.2% Triton X-100 in PBS for 5 min. After blocking with 1% bovine serum albumin (BSA) in PBS for 1 h at room temperature, samples were incubated with primary antibodies diluted in 1% BSA overnight at 4 °C.

Primary antibodies used included anti-CK7 (1:300, mouse), anti-dsRNA (1:500, mouse), anti–active caspase-3 (1:50, rabbit) and anti-pMLKL (1:200, rabbit). Samples were then incubated with appropriate secondary antibodies for 1 h at room temperature, followed by nuclear counterstaining with DAPI (Invitrogen). Confocal images were acquired using a Leica SP5 confocal microscope with a 40× oil-immersion objective.

Statistics. Statistical analyses were performed using a nonparametric, unpaired Mann–Whitney *U* test with GraphPad Prism 8.0 software. Data are presented as mean ± SD. Numbers of biological replicates are indicated in the figure legends. Statistical significance was defined as $P < 0.05$*, $P < 0.01$**, and $P < 0.001$***.

Data, Materials, and Software Availability. Study data are included in the article and/or supporting information.

ACKNOWLEDGMENTS. We are grateful to the patients for providing biomaterials and informed consent for research. We would like to thank the Erasmus MC Transplant Institute Biopsy4Research Facility at the Department of Surgery for sample processing, organoid initiation, storage, and distribution. Part of this work is supported by a VIDI grant (number 91719300 to Q.P.) from the Netherlands Organisation for Health Research and Development (ZonMw). L.J.W.v.d.L. gratefully acknowledges funding from Convergence Health Technology Flagship grant "Organ Transplantation" of the Erasmus MC and TU Delft (2022), European Union's Horizon 2020 research and innovation program grant NEOLIVER bioprinting (Grant no. 101191649), and Health-Holland Top Consortium for Knowledge and Innovation in Life Sciences & Health (TKI-LSH) grant RELOAD (project EMC-LSH19002). We thank S. U. Emerson (National Institute of Allergy and Infectious Diseases, NIH, USA) for providing the plasmids to generate HEV genomic RNA and the Allen Cell Collection for providing the H2B-GFP hiPSC line.

Author affiliations: [a]Department of Orthopaedics, Chongqing General Hospital, Chongqing University, Chongqing 401121, China; [b]Department of Surgery, Erasmus MC Transplant Institute, Erasmus University Medical Center, Rotterdam 3015GD, The Netherlands; [c]Department of Gastroenterology and Hepatology, Erasmus MC-University Medical Center, Rotterdam 3015GD, The Netherlands; [d]Department of Anatomy and Embryology, Leiden University Medical Center, Leiden 2333ZA, The Netherlands; [e]The Novo Nordisk Foundation Center for Stem Cell Medicine, reNEW, Leiden University Medical Center, Leiden 2333ZA, The Netherlands; and [f]Department of Biomechanical Engineering, Faculty of Mechanical Engineering, Biomaterials and Tissue Biomechanics, Delft University of Technology, Delft 2628CD, the Netherlands

1. N. Altan-Bonnet, M. Panigrahi, Nonlytic egress and transmission in the virus world. *Annu. Rev. Biochem.* **94**, 531–560 (2025).
2. D. Wodarz, J. P. Christensen, A. R. Thomsen, The importance of lytic and nonlytic immune responses in viral infections. *Trends Immunol.* **23**, 194–200 (2002).
3. V. A. Losay, B. Damania, Unraveling the Kaposi Sarcoma-Associated Herpesvirus (KSHV) lifecycle: An overview of latency, lytic replication, and KSHV-associated diseases. *Viruses* **17**, 177 (2025).
4. P. Li *et al.*, Recapitulating hepatitis E virus-host interactions and facilitating antiviral drug discovery in human liver-derived organoids. *Sci. Adv.* **8**, eabj5908 (2022).

5. N. Chew, J. Situ, S. Wu, W. Yao, S. Sridhar, Independent evaluation of cell culture systems for Hepatitis E Virus. *Viruses* **14**, 1254 (2022).
6. D. Todt *et al.*, Robust hepatitis E virus infection and transcriptional response in human hepatocytes. *Proc. Natl. Acad. Sci. U.S.A.* **117**, 1731–1741 (2020).
7. M. S. Hakim *et al.*, The global burden of hepatitis E outbreaks: A systematic review. *Liver Int.* **37**, 19–31 (2017).
8. R. Sehgal *et al.*, Impaired monocyte-macrophage functions and defective toll-like receptor signaling in hepatitis E virus-infected pregnant women with acute liver failure. *Hepatology* **62**, 1683–1696 (2015).
9. J. D. Debes, Z. M. A. Groothuismink, M. Doukas, R. A. de Man, A. Boonstra, Immune dissociation during acute hepatitis E infection. *Int. J. Infect. Dis.* **87**, 39–42 (2019).
10. A. Kumar *et al.*, Association of cytokines in hepatitis E with pregnancy outcome. *Cytokine* **65**, 95–104 (2014).
11. Y. Li *et al.*, Hepatitis E virus infection activates NOD-like receptor family pyrin domain-containing 3 inflammasome antagonizing interferon response but therapeutically targetable. *Hepatology* **75**, 196–212 (2022).
12. Y. Li *et al.*, Hepatitis E virus infection remodels the mature tRNAome in macrophages to orchestrate NLRP3 inflammasome response. *Proc. Natl. Acad. Sci. U.S.A.* **120**, e2304445120 (2023).
13. K. Liu *et al.*, Macrophage-augmented organoids recapitulate the complex pathophysiology of viral diseases and enable development of multitarget therapeutics.. *Nat. Biomed. Eng.* **9**, 1848–1868 (2025).
14. M. Merad, J. C. Martin, Pathological inflammation in patients with COVID-19: A key role for monocytes and macrophages. *Nat. Rev. Immunol.* **20**, 355–362 (2020).
15. S. Bedoui, M. J. Herold, A. Strasser, Emerging connectivity of programmed cell death pathways and its physiological implications. *Nat. Rev. Mol. Cell Biol.* **21**, 678–695 (2020).
16. L. R. Wong, S. Perlman, A confusion of pathways: Discerning cell death mechanisms in SARS-CoV-2 infection. *Sci. Immunol.* **9**, eadp8170 (2024).
17. K. Liang *et al.*, Initiator cell death event induced by SARS-CoV-2 in the human airway epithelium. *Sci. Immunol.* **9**, eadn0178 (2024).
18. Y. Gao *et al.*, Antivirals for treatment of severe influenza: A systematic review and network meta-analysis of randomised controlled trials. *Lancet* **404**, 753–763 (2024).
19. K. Yu *et al.*, Comprehensive transcriptomic analysis of cell lines as models of primary tumors across 22 tumor types.. *Nat. Commun.* **10**, 3574 (2019).
20. B. Artegiani, D. Hendriks, Organoids from pluripotent stem cells and human tissues: When two cultures meet each other. *Dev. Cell* **60**, 493–511 (2025).
21. G. Xu *et al.*, Macrophage-augmented intestinal organoids model virus-host interactions in enteric viral diseases and facilitate therapeutic development. *Nat. Commun.* **16**, 4475 (2025).
22. W. Wang *et al.*, The RNA genome of Hepatitis E virus robustly triggers an antiviral interferon response. *Hepatology* **67**, 2096–2112 (2018).
23. A. Beer *et al.*, Chronic Hepatitis E is associated with cholangitis. *Liver Int.* **39**, 1876–1883 (2019).
24. F. J. M. Roos *et al.*, Human branching cholangiocyte organoids recapitulate functional bile duct formation. *Cell Stem Cell* **29**, 776–794.e13 (2022).
25. A. Marsee *et al.*, Building consensus on definition and nomenclature of hepatic, pancreatic, and biliary organoids. *Cell Stem Cell* **28**, 816–832 (2021).
26. B. Wang, X. J. Meng, Hepatitis E virus: Host tropism and zoonotic infection. *Curr. Opin. Microbiol.* **59**, 8–15 (2021).
27. P. Shukla *et al.*, Cross-species infections of cultured cells by hepatitis E virus and discovery of an infectious virus-host recombinant. *Proc. Natl. Acad. Sci. U.S.A.* **108**, 2438–2443 (2011).
28. J. Shi *et al.*, Cleavage of GSDMD by inflammatory caspases determines pyroptotic cell death. *Nature* **526**, 660–665 (2015).
29. X. Cao, F. E. Hil, C. L. Mummery, V. V. Orlova, Generation and functional characterization of monocytes and macrophages derived from human induced pluripotent stem cells. *Curr. Protoc. Stem Cell Biol.* **52**, e108 (2020).
30. Y. Debing *et al.*, Ribavirin inhibits in vitro Hepatitis E virus replication through depletion of cellular GTP pools and is moderately synergistic with alpha interferon. *Antimicrob. Agents Chemother.* **58**, 267–273 (2014).
31. Q. He *et al.*, Immunocompromised rabbit model of chronic HEV reveals liver fibrosis and distinct efficacy of different vaccination strategies. *Hepatology* **76**, 788–802 (2022).
32. N. Kamar *et al.*, Ribavirin for chronic hepatitis E virus infection in transplant recipients. *N. Engl. J. Med.* **370**, 1111–1120 (2014).
33. A. Zahid, B. Li, A. J. K. Kombe, T. Jin, J. Tao, Pharmacological inhibitors of the NLRP3 inflammasome. *Front. Immunol.* **10**, 2538 (2019).
34. R. C. Group *et al.*, Dexamethasone in hospitalized patients with Covid-19. *N. Engl. J. Med.* **384**, 693–704 (2021).
35. J. L. Casanova, L. Abel, Mechanisms of viral inflammation and disease in humans. *Science* **374**, 1080–1086 (2021).
36. M. Peiseler *et al.*, Kupffer cell-like syncytia replenish resident macrophage function in the fibrotic liver. *Science* **381**, eabq5202 (2023).
37. T. Recaldin *et al.*, Human organoids with an autologous tissue-resident immune compartment. *Nature* **633**, 165–173 (2024).
38. L. E. Wagar *et al.*, Modeling human adaptive immune responses with tonsil organoids. *Nat. Med.* **27**, 125–135 (2021).
39. Z. W. Wagoner *et al.*, Systems immunology analysis of human immune organoids identifies host-specific correlates of protection to different influenza vaccines. *Cell Stem Cell* **32**, 529–546.e26 (2025).
40. D. Wang, R. Villenave, N. Stokar-Regenscheit, H. Clevers, Human organoids as 3D in vitro platforms for drug discovery: Opportunities and challenges. *Nat. Rev. Drug Discov.* **25**, 204–226 (2025), 10.1038/s41573-025-01317-y.
41. R. Medzhitov, The spectrum of inflammatory responses. *Science* **374**, 1070–1075 (2021).
42. B. Sundaram *et al.*, NLRC5 senses NAD(+) depletion, forming a PANoptosome and driving PANoptosis and inflammation. *Cell* **187**, 4061–4077.e17 (2024).
43. M. Zheng, R. Karki, P. Vogel, T. D. Kanneganti, Caspase-6 Is a Key Regulator of Innate Immunity, Inflammasome Activation, and Host Defense. *Cell* **181**, 674–687.e13 (2020).
44. A. Franz *et al.*, Early ribavirin for Hepatitis E virus infection in patients receiving immunosuppressive therapy: A retrospective, observational study. *J. Int. Med. Res.* **51**, 3000605231187941 (2023).
45. Z. Ma, R. A. de Man, N. Kamar, Q. Pan, Chronic hepatitis E: Advancing research and patient care. *J. Hepatol.* **77**, 1109–1123 (2022).
46. L. Yuan *et al.*, Dexamethasone ameliorates severe pneumonia but slightly enhances viral replication in the lungs of SARS-CoV-2–infected Syrian hamsters. *Cell Mol. Immunol.* **19**, 290–292 (2022).
47. A. Gautam *et al.*, Necroptosis blockade prevents lung injury in severe influenza. *Nature* **628**, 835–843 (2024).